

# Fresnel Microfacet BRDF: Unification of Polari-Radiometric Surface-Body Reflection Supplementary Material

Tomoki Ichikawa    Yoshiki Fukao    Shohei Nobuhara    Ko Nishino  
Graduate School of Informatics, Kyoto University  
<https://vision.ist.i.kyoto-u.ac.jp/>

Section / figure / table / equation numbers prefixed with “A” refer to those in this supplemental material. Others refer to those in the main text unless specified otherwise.

## A.1. Polarization

Within the temporal span of an observation (*e.g.*, image exposure), the observed light may consist of a collection of linearly polarized light of varying magnitudes, *i.e.*, elliptically distributed polarization. If we capture this partially polarized light with a polarization filter, the observed intensity becomes a function of the filter angle  $\phi_c$ :

$$I(\phi_c) = \bar{I} + \rho \bar{I} \cos(2\phi_c - 2\phi), \quad (\text{A.1})$$

where  $I_{\max}$  and  $I_{\min}$  are the intensities in the major and minor axes of the ellipse,  $\bar{I}$  is the average intensity ( $= \frac{I_{\max} + I_{\min}}{2}$ ) and  $\rho = \frac{I_{\max} - I_{\min}}{I_{\max} + I_{\min}}$  is the degree of linear polarization (DoLP). The angle  $\phi$  is called the angle of linear polarization (AoLP) which is the angle the major axis of the ellipse makes in the image plane.

When light is reflected at a surface point, the light either mirror reflects or transmits into the surface. This can be described by the Fresnel equations, *i.e.*, Fresnel reflectance and transmittance. When light is mirror reflected, it is linearly polarized in the direction perpendicular to the plane of reflection (*i.e.*, s-polarized). Similarly, when light is transmitted into the surface, it is linearly polarized in the direction parallel to the plane of reflection (*i.e.*, p-polarized).

Let us express these polarization behaviors with Stokes vectors which succinctly summarizes polarization states. In the case of linear polarization, the Stokes vector is computed from the intensity at filter angles  $0, \pi/4, \pi/2$ , and  $3/4\pi$ ,

$$\mathbf{s} = \begin{bmatrix} s_0 \\ s_1 \\ s_2 \\ 0 \end{bmatrix} = \begin{bmatrix} I(0) + I(\frac{\pi}{2}) \\ I(0) - I(\frac{\pi}{2}) \\ I(\frac{\pi}{4}) - I(\frac{3}{4}\pi) \\ 0 \end{bmatrix} = \begin{bmatrix} 2\bar{I} \\ 2\bar{I}\rho \cos \phi \\ 2\bar{I}\rho \sin \phi \\ 0 \end{bmatrix}. \quad (\text{A.2})$$

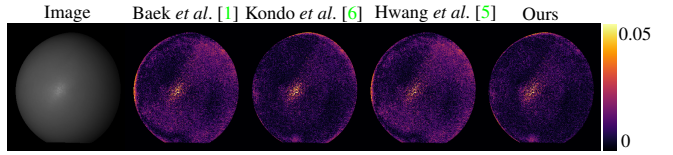


Figure A.1. DoLP errors of different pBRDF models. In body reflection dominant regions, our model achieves smallest errors.

The DoLP can be extracted from the Stokes vector

$$\rho = \frac{\sqrt{s_1^2 + s_2^2}}{s_0}. \quad (\text{A.3})$$

We do not model circular polarization as it cannot be measured easily.

The polarization transform by reflection and transmittance is expressed with their corresponding Mueller matrix  $\mathbf{M}$

$$\mathbf{s}_o = \mathbf{M} \mathbf{s}_i, \quad (\text{A.4})$$

where  $\mathbf{s}_i$  is the Stokes vector of incident light and  $\mathbf{s}_o$  is the Stokes vector of reflected or transmitted light.

In our model, we need the Mueller matrices of surface reflection, Fresnel transmittance, subsurface scattering, and rotation of a Stokes vector. The Mueller matrix of surface reflection  $\mathbf{R}$  is given by

$$\mathbf{R}(\theta) = \begin{bmatrix} R_+ & R_- & 0 & 0 \\ R_- & R_+ & 0 & 0 \\ 0 & 0 & R_\times \cos \delta & 0 \\ 0 & 0 & 0 & R_\times \cos \delta \end{bmatrix}, \quad (\text{A.5})$$

where  $R_\pm = \frac{R_s \pm R_p}{2}$ ,  $R_\times = \sqrt{R_s R_p}$ ,  $\theta$  is the incident light angle, and  $\cos \delta$  is  $-1$  when  $\theta$  is less than the Brewster’s angle and  $1$  otherwise.  $R_s$  and  $R_p$  are the Fresnel coefficients

$$R_s(\theta) = \left( \frac{\cos \theta - \mu \cos \theta_t}{\cos \theta + \mu \cos \theta_t} \right)^2, \quad R_p(\theta) = \left( \frac{\mu \cos \theta - \cos \theta_t}{\mu \cos \theta + \cos \theta_t} \right)^2, \quad (\text{A.6})$$

where  $\mu$  is the index of refraction of the object material, and  $\theta_t$  is given by Snell’s law  $\theta_t = \sin^{-1} \left( \frac{1}{\mu} \sin \theta \right)$ . The polarization transform by Fresnel transmittance is expressed with

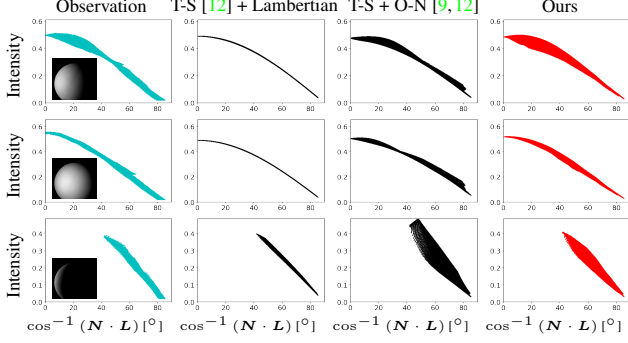


Figure A.2. Fitting results for a plaster sphere. The graphs show observed and rendered graphs under three different lighting conditions. The RMSE of each model is 0.0325, 0.0341, and 0.0245, respectively. Our model subsumes and can accurately represent Lambertian reflection.

the Fresnel coefficients

$$\mathbf{T}(\theta) = \begin{bmatrix} T_+ & T_- & 0 & 0 \\ T_- & T_+ & 0 & 0 \\ 0 & 0 & T_\times & 0 \\ 0 & 0 & 0 & T_\times \end{bmatrix}, \quad (\text{A.7})$$

where  $T_\pm = \frac{T_s \pm T_p}{2}$ ,  $T_\times = \sqrt{T_s T_p}$ , and  $\theta$  is the incident light angle.  $T_s$  and  $T_p$  are the Fresnel coefficients

$$T_s(\theta) = 1 - R_s(\theta), T_p(\theta) = 1 - R_p(\theta). \quad (\text{A.8})$$

Subsurface scattering depolarizes transmitted light, and its Mueller matrix is given by

$$\mathbf{D}_p \left( \frac{k_b}{\pi} \right) = \begin{bmatrix} \frac{k_b}{\pi} & 0 & 0 & 0 \\ 0 & 0 & 0 & 0 \\ 0 & 0 & 0 & 0 \\ 0 & 0 & 0 & 0 \end{bmatrix}, \quad (\text{A.9})$$

where  $k_b$  is the body reflection albedo. Rotation matrix of Stokes vector is given by

$$\mathbf{C}(\varphi) = \begin{bmatrix} 1 & 0 & 0 & 0 \\ 0 & \cos(2\varphi) & -\sin(2\varphi) & 0 \\ 0 & \sin(2\varphi) & \cos(2\varphi) & 0 \\ 0 & 0 & 0 & 1 \end{bmatrix}, \quad (\text{A.10})$$

where  $\varphi$  is the rotation angle.

## A.2. Analysis of Masking and Shadowing Term

Let us analyze in detail the masking and shadowing term  $M(\mathbf{n}, \mathbf{n}_i)$  in Eq. (16) in the main paper that takes into account light transport within the microgeometry  $S'(\mathbf{p}, \mathbf{p}_i)$ . The product of the masking and shadowing function  $G_m^b(\mathbf{p})G_s^b(\mathbf{p}_i)$  has been studied as joint masking-shadowing functions [4] when  $\mathbf{p} = \mathbf{p}_i$ . We follow the widely used separable masking-shadowing function which we use for the surface reflection model and extend it to the

case of  $\mathbf{p} \neq \mathbf{p}_i$ . The separable masking-shadowing model assumes that  $G_m^b(\mathbf{p})$  and  $G_s^b(\mathbf{p})$  are independent for  $\mathbf{p}$ . Extending this assumption, we assume  $G_m^b(\mathbf{p})$  and  $G_s^b(\mathbf{p}_i)$  are independent of the distance between  $\mathbf{p}$  and  $\mathbf{p}_i$ . From this assumption, the masking-shadowing function  $G_m^b(\mathbf{p})G_s^b(\mathbf{p}_i)$  is independent of the distance between  $\mathbf{p}$  and  $\mathbf{p}_i$ . Since the light transport  $S'(\mathbf{p}, \mathbf{p}_i)$  largely depends on the distance between  $\mathbf{p}$  and  $\mathbf{p}_i$ , we can assume that  $G_m^b(\mathbf{p})G_s^b(\mathbf{p}_i)$  and  $S'(\mathbf{p}, \mathbf{p}_i)$  have no correlation for  $\mathbf{p}$  and  $\mathbf{p}_i$ . The average of their product in Eq. (16) becomes the product of each average due to statistical independence between  $G_m^b(\mathbf{p})G_s^b(\mathbf{p}_i)$  and  $S'(\mathbf{p}, \mathbf{p}_i)$ , and that of  $G_m^b(\mathbf{p})$  and  $G_s^b(\mathbf{p}_i)$ . We obtain

$$M(\mathbf{n}, \mathbf{n}_i) = G_m(\mathbf{n})G_s(\mathbf{n}_i)\overline{S'}(\mathbf{n}, \mathbf{n}_i), \quad (\text{A.11})$$

where  $G_m(\mathbf{n})$ ,  $G_s(\mathbf{n}_i)$ , and  $\overline{S'}(\mathbf{n}, \mathbf{n}_i)$  are the average of  $G_m^b(\mathbf{p})$ ,  $G_s^b(\mathbf{p}_i)$ , and  $S'(\mathbf{p}, \mathbf{p}_i)$  for  $\mathbf{p}$  and  $\mathbf{p}_i$ , respectively.

We analyze  $\overline{S'}(\mathbf{n}, \mathbf{n}_i)$  which is the average of light transport incident on  $\mathbf{p}_i$  from  $\mathbf{L}$  and outgoing from  $\mathbf{p}$  to  $\mathbf{V}$  under the surface for all combinations of  $\mathbf{p}$  and  $\mathbf{p}_i$ . Light transported from  $\mathbf{p}_i$  to  $\mathbf{p}$  may be directional depending on the direction from  $\mathbf{p}_i$  to  $\mathbf{p}$ . However, when the direction from  $\mathbf{p}_i$  to  $\mathbf{p}$  is random for  $\mathbf{p}$  in  $A_n$  and  $\mathbf{p}_i$  in  $A_{n_i}$ , the average light is not directional. Moreover, sufficient scattering weakens the effect of the incident direction  $\mathbf{L}$ . We can thus safely assume that  $\overline{S'}(\mathbf{n}, \mathbf{n}_i)$  does not depend on  $\mathbf{L}$  and  $\mathbf{V}$ .

The masking and shadowing function by Smith [11] assume that there is no correlation between the microfacet normals of different points on the microgeometry. In this case,  $\overline{S'}(\mathbf{n}, \mathbf{n}_i)$  is constant for  $\mathbf{n}$  and  $\mathbf{n}_i$ . It, however, can also represent correlated surfaces [2] and we can safely use it as an approximation.

## A.3. Additional Results: Polarimetric Model Accuracy

Figure A.1 shows the DoLP error map of the fitting results of the fourth row in Fig. 4 in the main paper. The lighting condition is different from Fig. 4. The DoLP errors of our model are the smallest among these different pBRDF models near the edges of the sphere where body reflection is dominant. This result shows that our model can represent the polarimetric behavior of body reflection more accurately.

## A.4. Additional Results: Radiometric Model Accuracy

Figure A.2 shows fitting results for a plaster sphere which is more or less a pure Lambertian object. We fit each model to 10 images captured under different lighting conditions and compute the root-mean-square error (RMSE) for all images. The RMSEs of Torrance-Sparrow [12] plus Lambertian model, Torrance-Sparrow [12] plus Oren-Nayar

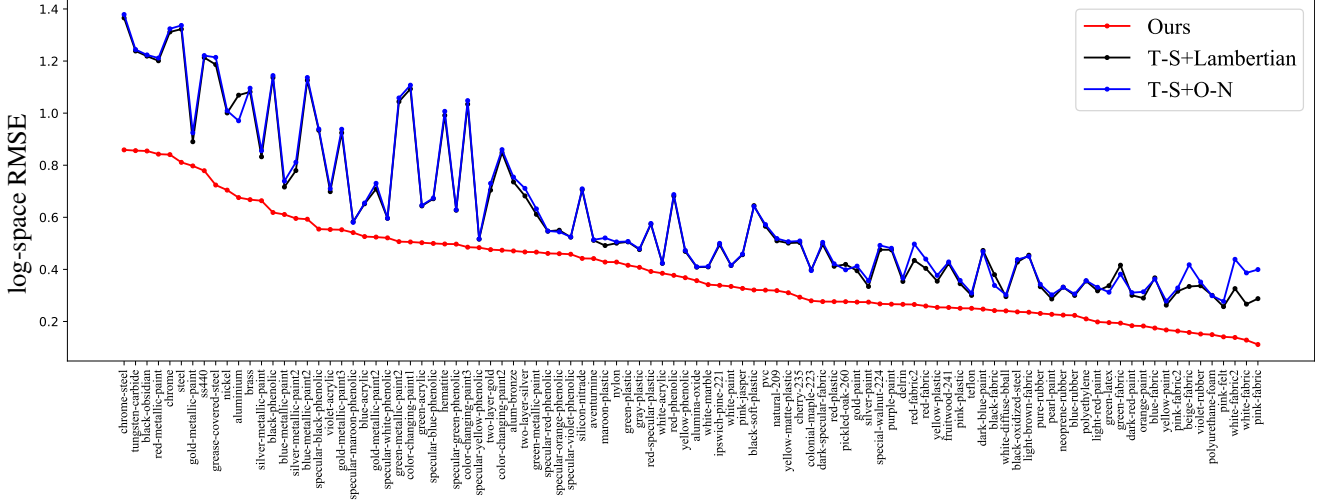


Figure A.3. Evaluation on the MERL dataset shown in log-space root-mean-square error for each material. The results are sorted by the error magnitude of our model. Our model expresses most measured BRDFs more accurately than other physically-based BRDF models.

[9] model, and our model are 0.0325, 0.0341, and 0.0245, respectively. Our model accurately explains Lambertian reflection with Fresnel transmission and microgeometry light transport by mirror microfacets without relying on the physically implausible Lambertian microfacet assumption.

We also evaluate the radiometric accuracy of our FMBRDF model with the MERL dataset [8]. Figure A.3 shows fitting results in log-space root-mean-square error [7] of our model and other radiometric BRDF models for each material. The RMSE in log-space is given by

$$E_{\ell\text{-RMSE}} = \sqrt{\frac{\sum_{\theta_h, \theta_d, \phi_d} (\log f(\theta_h, \theta_d, \phi_d) - \log \hat{f}(\theta_h, \theta_d, \phi_d))^2}{N}}, \quad (\text{A.12})$$

where  $N$  is the number of sampled BRDFs,  $\theta_h$ ,  $\theta_d$ , and  $\phi_d$  are half and difference angles of Rusinkiewicz parameterization [10],  $f(\theta_h, \theta_d, \phi_d)$  is a measured BRDF, and  $\hat{f}(\theta_h, \theta_d, \phi_d)$  is the fit BRDF model. The fitting errors of our FMBRDF model are the smallest compared with other physically-based BRDF models for all materials.

## A.5. Application: Geometry Reconstruction

We demonstrate the use of FMBRDF for 3D geometry reconstruction of an object with an unknown BRDF by jointly estimating the BRDF and geometry. We capture the target object under different point source directions but from the same viewpoint. We first obtain initial estimates of surface normals by using the Lambertian model (i.e., classic photometric stereo). Using these inaccurate surface nor-

mals, we recover the FMBRDF parameter values. Once we have these FMBRDF parameters, we update the surface geometry and iterate this alternating updates of surface normal and FMBRDF parameters. After the convergence of alternating updates, we jointly optimize the surface geometry and FMBRDF parameters. For robust geometry reconstruction, we propagate the surface normal at each pixel to adjacent pixels to minimize the loss function. We obtain the final result by iterating the joint optimization and the surface normal propagation.

The loss function for estimating the FMBRDF parameters and surface normals consists of a radiance loss  $E_{\text{rad}}$ , a DoLP loss  $E_{\text{DoLP}}$ , a polarization loss  $E_{s_1, s_2}$ , and a smoothness loss  $E_s$ . Each loss is defined by

$$E_{\text{rad}} = \frac{1}{\sum_{k=1}^K M_k} \sum_{k=1}^K \sum_{i=1}^{M_k} (\bar{s}_{i0}^k - s_{i0}^k)^2, \quad (\text{A.13})$$

$$E_{\text{DoLP}} = \frac{1}{\sum_{k=1}^K M_k} \sum_{k=1}^K \sum_{i=1}^{M_k} (\bar{\rho}_i^k - \rho_i^k)^2, \quad (\text{A.14})$$

$$E_{s_1, s_2} = \frac{1}{\sum_{k=1}^K M_k} \sum_{k=1}^K \sum_{i=1}^{M_k} \{(\bar{s}_{i1}^k - s_{i1}^k)^2 + (\bar{s}_{i2}^k - s_{i2}^k)^2\}, \quad (\text{A.15})$$

$$E_s = \frac{1}{\sum_{i=1}^M |\mathcal{N}(i, r)|} \sum_{i=1}^M \sum_{\mathbf{n}'_i \in \mathcal{N}(i, r)} \frac{1 - \mathbf{n}_i \cdot \mathbf{n}'_i}{2}, \quad (\text{A.16})$$

where  $M$  is the number of pixels of the object,  $M_k$  is the number of pixels of the object masked with radiance in the

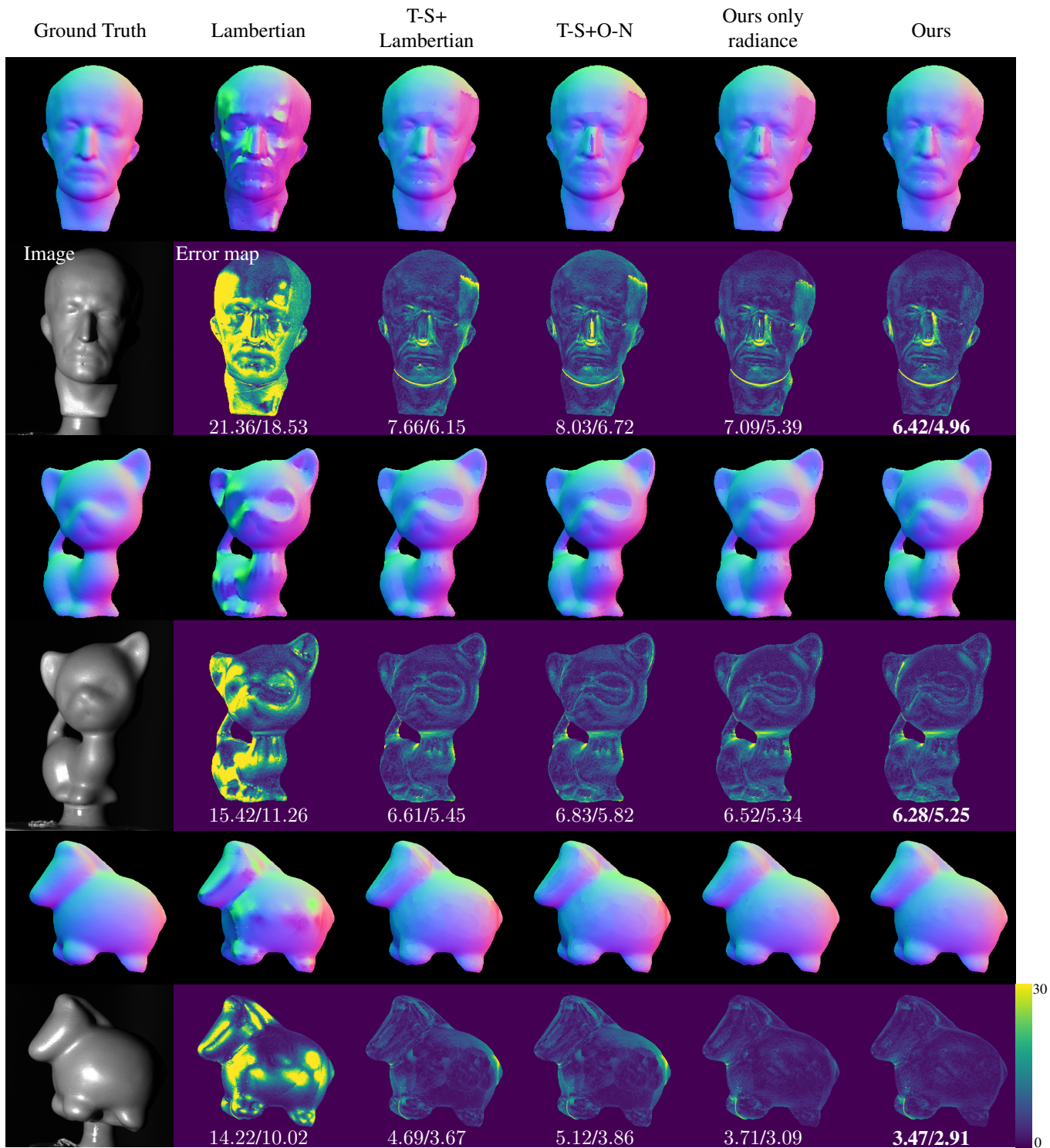


Figure A.4. Reconstruction results of various objects with unknown BRDFs. The numbers report the mean/median angular normal errors in degrees. Our FMBRDF achieves higher accuracy and robustness in geometry reconstruction, mainly as it can leverage both radiometric and polarimetric information.

image  $k$ ,  $K$  is the number of polarimetric images,  $\bar{s}_{i0}^k$ ,  $\bar{s}_{i1}^k$ , and  $\bar{s}_{i2}^k$  are each of the elements of the observed Stokes vec-

tor at pixel  $i$  in image  $k$ ,  $s_{i0}$ ,  $s_{i1}$ , and  $s_{i2}$  are each of the elements of the rendered Stokes vector at pixel  $i$  in image  $k$ ,  $\bar{\rho}_i^k$  and  $\rho_i^k$  are the observed and rendered DoLPs at pixel  $i$  in image  $k$ , respectively,  $\mathbf{n}_i$  is the estimated surface normal at pixel  $i$ ,  $\mathcal{N}(i, r)$  is the set of surface normals in the  $(2r+1) \times (2r+1)$  window centered at pixel  $i$ , and  $|\mathcal{N}(i, r)|$  is the cardinality of  $\mathcal{N}(i, r)$ .

The loss functions for the estimation of the FMBRDF parameters and the surface normals and the joint estimation are defined by

$$\min_{\mu, r_k, k_s, \alpha, \beta, \kappa} E_{\text{Rad}} + \lambda_{\text{DoLP}} E_{\text{DoLP}}, \quad (\text{A.17})$$

$$\min_{\mathbf{n}_1, \dots, \mathbf{n}_M} E_{\text{Rad}} + \lambda_{s_1, s_2} E_{s_1, s_2} + \lambda_s E_s, \quad (\text{A.18})$$

$$\min_{\mathbf{n}_1, \dots, \mathbf{n}_M, \mu, r_k, k_s, \alpha, \beta, \kappa} E_{\text{Rad}} + \lambda_{\text{DoLP}} E_{\text{DoLP}} + \lambda_{s_1, s_2} E_{s_1, s_2}, \quad (\text{A.19})$$

respectively. The weights for DoLP and polarization losses are  $\lambda_{\text{DoLP}} = 0.1$  and  $\lambda_{s_1, s_2} = 5.0$ , respectively. We decrease the weight  $\lambda_s$  and size  $r$  of the smoothness loss as the alternating optimization progresses. We set  $\lambda_s = 0.05$  and  $r = 5$  for the first three iterations,  $\lambda_s = 0.03$  and  $r = 3$  for the next three iterations, and  $\lambda_s = 0.01$  and  $r = 1$  after that. We use the loss function of the joint estimation for surface normal propagation.

To render the Stokes vector captured with a perspective polarization camera, following [3], we compute AoLP as the projection of polarization direction of  $\mathbf{s}_s + \mathbf{s}_b$  in a 3D space onto the image plane. Other BRDF models use radiance values in a similar alternating minimization to jointly estimate their parameter values and surface normals.

Figure A.4 shows 3D geometry reconstructions of various objects with unknown BRDFs. Our model clearly reconstructs the shape more accurately and robustly thanks to the radiometric and polarimetric accuracy of our model.

## A.6. Limitation

Our model is derived for dielectric surfaces and linear polarization, and it cannot represent metallic surfaces and circular polarization. Our model cannot represent retro-reflection, as seen in the right graph of Fig. 6 in the main paper, and asperity scattering. Since we use a generalized normal distribution function as a microfacet distribution, our model cannot represent an anisotropic surface. We plan to explore modeling these in our future work.

## References

- [1] Seung-Hwan Baek, Daniel S. Jeon, Xin Tong, and Min H. Kim. Simultaneous Acquisition of Polarimetric SVBRDF and Normals. *ACM TOG*, 37:1 – 15, 2018. 1
- [2] Christophe Bourlier, Joseph Saillard, and Gerard Berginc. Effect of Correlation Between Shadowing and Shad-

- owed Points on the Wagner and Smith Monostatic One-Dimensional Shadowing Functions. *IEEE Transactions on Antennas and Propagation*, 48(3):437–446, 2000. 2
- [3] Guangcheng Chen, Li He, Yisheng Guan, and Hong Zhang. Perspective Phase Angle Model for Polarimetric 3D Reconstruction. In *ECCV*, pages 398–414. Springer, 2022. 5
- [4] Eric Heitz. Understanding the Masking-Shadowing Function in Microfacet-Based BRDFs. *Journal of Computer Graphics Techniques (JCGT)*, 3(2):48–107, June 2014. 2
- [5] Inseung Hwang, Daniel S Jeon, Adolfo Muñoz, Diego Gutierrez, Xin Tong, and Min H Kim. Sparse Ellipsometry: Portable Acquisition of Polarimetric SVBRDF and Shape with Unstructured Flash Photography. *ACM TOG*, 41(4):1–14, 2022. 1
- [6] Yuhi Kondo, Taishi Ono, Legong Sun, Yasutaka Hirasawa, and Jun Murayama. Accurate Polarimetric BRDF for Real Polarization Scene Rendering. In *ECCV*, pages 220–236. Springer, 2020. 1
- [7] Stephen Lombardi and Ko Nishino. Reflectance and Illumination Recovery in the Wild. *IEEE TPAMI*, 38(1):129–141, 2016. 3
- [8] Wojciech Matusik, Hanspeter Pfister, Matt Brand, and Leonard McMillan. A Data-Driven Reflectance Model. *ACM TOG*, 22(3):759–769, July 2003. 3
- [9] Michael Oren and Shree K. Nayar. Generalization of the Lambertian Model and Implications for Machine Vision. *International Journal of Computer Vision*, 14:227–251, 1995. 2, 3
- [10] Szymon M Rusinkiewicz. A New Change of Variables for Efficient BRDF Representation. In *Eurographics Workshop on Rendering Techniques*, pages 11–22. Springer, 1998. 3
- [11] Bruce Smith. Geometrical Shadowing of a Random Rough Surface. *IEEE transactions on antennas and propagation*, 15(5):668–671, 1967. 2
- [12] Kenneth E Torrance and Ephraim M Sparrow. Theory for Off-Specular Reflection From Roughened Surfaces. *Josa*, 57(9):1105–1114, 1967. 2